NJC

Accepted Manuscript

This is an *Accepted Manuscript*, which has been through the Royal Society of Chemistry peer review process and has been accepted for publication.

Accepted Manuscripts are published online shortly after acceptance, before technical editing, formatting and proof reading. Using this free service, authors can make their results available to the community, in citable form, before we publish the edited article. We will replace this *Accepted Manuscript* with the edited and formatted *Advance Article* as soon as it is available.

You can find more information about *Accepted Manuscripts* in the Information for Authors.

Please note that technical editing may introduce minor changes to the text and/or graphics, which may alter content. The journal's standard Terms & Conditions and the Ethical guidelines still apply. In no event shall the Royal Society of Chemistry be held responsible for any errors or omissions in this *Accepted Manuscript* or any consequences arising from the use of any information it contains.

ROYAL SOCIETY OF CHEMISTRY

www.rsc.org/njc

New Journal of Chemistry

ARTICLE

Impact of chabazite SSZ-13 textural properties and chemical composition on CO_2 adsorption applications

Received 00th January 20xx,
Accepted 00th January 20xx

DOI: 10.1039/x0xx00000x

www.rsc.org/

Sebastian Prodinger,[a] Rama S. Vemuri,[b] Tamas Varga,[c] B. Peter McGrail,[b] Radha Kishan Motkuri,[b,*] and Miroslaw A. Derewinski[a,*]

Chabazite SSZ-13 samples with varying silica content (Si/Al from 5 to ~20) were synthesized under both stirring and static conditions to obtain material with changing particle size and morphology and thoroughly analysed with various characterization techniques. The role of particle size and chemical compositions on CO_2 and N_2 adsorption measurements was investigated. The Si/Al ratio played a major role for CO_2 adsorption; Al-rich SSZ-13 demonstrated a higher CO_2 uptake than Al-poor material. This was attributed to the high density of active charged species in the chabazite cage. Particle size also played a role in the sorption capacities; smaller particles, obtained under stirring conditions, showed enhanced CO_2 uptakes compared to larger particles of similar chemical composition. This was associated with a higher contribution of micropores containing active sites for CO_2 adsorption.

Introduction

The global-scale problem of deteriorating climate has mandated the reduction in greenhouse gas emission.[1-4] A significant amount of CO_2 is generated in coal-fired power plants, required to meet a large share of the worldwide energy demand. Along with the development of green energy sources, the long-term strategy is to integrate carbon sequestration and capture technology into coal- and gas-fired power plants and other conventional fossil-based energy sources. Current states of the art in carbon capture are the oxyfuel technology, amine scrubbing, ionic liquid solvation and solid adsorbents such as porous carbon, metal-organic frameworks (MOFs), and zeolites.[5-10] MOFs and zeolites are lucrative for the capture of carbon from power plant flue gases because of their selectivity, fast kinetics, and quick regeneration for reuse.[11-14]

Zeolites are naturally occurring microporous aluminosilicates. They can also be synthesized under hydrothermal conditions typically using silica and alumina sources in alkaline conditions with the help of structure-directing agents.[15, 16] The inherent three-dimensional network of microporous channels and voids of zeolites generates their capability for a large number of sorption and separation applications.[17] In addition, the incorporation of aluminium and resulting generation of a negative charge necessitates the use of charge-balancing ions. Brønsted acidity, as a result of charge-balancing protons, gives zeolites a wide array of applications in catalysis.[18] The high thermal and chemical stability in addition to narrow pore openings and relatively cheap manufacturing costs make zeolites interesting candidates for membrane applications in gas-mixture separations, especially CO_2 separation.[19-21] Furthermore, MOFs have also gained a lot of attention for sorption and separation applications.[22-24] This can be mainly attributed to their advantageous use in low-pressure CO_2 capture applications, relevant for separation of CO_2 from flue gases.[2, 25] However, a recent report by Bae et al. on zeolite A exchanged with calcium showed the continued relevance of zeolites for CO_2 sorption/separation applications (4.22 mmol/cm^3 and 2.79 mmol/g).[26] CaA was found to have superior performance in CO_2 capture, surpassing the sorption capacity of Mg-MOF-74 (3.88 mmol/cm^3 and 4.26 mmol/g), considered to be one of the best-performing MOFs.[26, 27]

Early studies reported cage and window type zeolites, such as faujasite type frameworks (NaX, NaY zeolite), to be the most promising adsorbent for CO_2 capture at low feed conditions.[28] Yet, recent studies showed zeolites with cages connected with narrow eight-membered rings (8MRs) to have the best CO_2 adsorption characteristics. These characteristics were linked to the close match of the oxygen window diameter and zeolite pore aperture with the kinetic diameter of the CO_2 molecule.[29, 30] Computationally, through configurational Monte Carlo simulation and molecular dynamics studies, Krishna et al. demonstrated that zeolite frameworks with narrow windows

[a] Institute of Integrated Catalysis, Physical Sciences Division, Pacific Northwest National Laboratory (PNNL), Richland, Washington 99352, USA. Email:Miroslaw.Derewinski@pnnl.gov
[b] Hydrocarbon Processing Group, Energy and Environment Directorate, Pacific Northwest National Laboratory (PNNL), Richland, WA 99352, USA. Email: Radhakishan.Motkuri@pnnl.gov
[c] Environmental Molecular Sciences Laboratory, Pacific Northwest National Laboratory (PNNL), Richland, WA 99352, USA.

† Electronic Supplementary Information (ESI) available: XRD patterns, HIM images, particle size distribution, ^{27}Al MAS NMR spectra, N_2 physisorption isotherms, pore size distribution and CO_2 and N_2 adsorption measurements. See DOI: 10.1039/x0xx00000x

of 3.5Å – 4.5Å (e.g., CHA, ITQ-29) yield the highest selectivity for CO_2 separation (S_{diff} >> 1).[31] Accordingly, Lobo et al. reported a series of papers on selective sorption and separation of CO_2 using chabazite SSZ-13 zeolite.[32-35]

SSZ-13 is a small-pore zeolite made up of the chabazite (CHA) framework type composed of double six-membered ring (DR6) building units, connected via four-membered rings. As a result, large ellipsoidal CHA cavities (~7.3 Å x 12 Å)[36] are formed and are accessed by 8MR windows with an approximate free aperture of 3.8 Å.[37] More importantly, most cations in the chabazite framework are fully accessible to guest molecules such as CO_2.[33] This is in contrast to zeolites A, X, and Y, where large fractions of cations are located in sodalite cages, which are not directly accessible to the guest molecules.[33] Control of the particle size of this highly interesting material has been an on-going challenge, and recent work by Bohström et al. illustrated the facets influencing particle size during synthesis.[38] They synthesized high-silica (Si/Al 50) SSZ-13 crystals ranging from 200 nm to 4.5 µm.

Here, we report the investigation of CO_2 and N_2 adsorption properties in chabazite SSZ-13 zeolite, the impact of textural properties of the material, and the role of chemical composition, more specifically the aluminium content of the zeolite. Our work describes the synthesis of eight different materials with varying Si/Al ratios and various particle sizes, ranging from less than 250 nm to as large as 17 µm. By varying the Si/Al ratio of ~5, ~9, ~13, and ~20, the number of aluminium atoms per unit cell is changed from approximately 2.4 to 1.3, 0.9, and 0.6 respectively. Furthermore, the chosen synthesis method allowed for a variation in textural properties such as decreasing particle size, which will be shown to have an influence on the adsorption performance and uptake of CO_2.

Experimental

Synthesis of SSZ-13

As-made material. SSZ-13 was synthesized by modifying a procedure reported by Gao et al.[39] The gel composition was as follows: $20TMAdaOH:10Na_2O:xAl_2O_3:100SiO_2:4400H_2O$ with the molar content of Al_2O_3 being varied from 1.43 (Si/Al_{gel} 35) to 8.3 (Si/Al_{gel} 6). NaOH (Aldrich) was dissolved in H_2O followed by the sequential addition of $Al(OH)_3$ (54% Al_2O_3, Aldrich) and structure-directing agent N,N,N-trimethyladamantylammonium hydroxide (TMAda-OH) (24.8 wt% in H_2O solution, Sachem Zeogen 2825). The solution was stirred until it became clear. Then fumed silica (0.007 µm average particle size, Aldrich) was slowly added and the gel was aged at room temperature for close to 24 h. Upon completion, a Teflon-lined autoclave fitted with a Teflon stir bar was charged with a portion of the aged gel, placed upon a stir plate, and heated to 160°C. The remaining gel was placed in a Teflon-lined autoclave and kept in an oven at 160°C under static conditions. Static synthesis typically lasted around 10 days. Stirring conditions led to a faster crystallization rate with completion requiring only 4 days at 160°C. Once the synthesis came to an end, the suspension was separated via centrifugation and the solid residue was washed several times with deionized water until a neutral pH was obtained. The as-made material was then dried in an oven overnight at 80°C.

Calcined Na-form: The as-made material was calcined in synthetic air at 200°C for 1 h followed by 8 h at 550°C. The heating rate was 1°C/min.

Sample characterization

Powder X-ray diffraction (PXRD). A Rigaku Mini Flex II benchtop X-ray diffractometer using a Cu-Kα radiation of 0.154056 nm (30 kV and 15 mA) was used to obtain XRD patterns. The sample was placed in a powder sample holder at ambient conditions and a pattern was collected from 2θ range of 5-65°. The step size was 2°/min.

Lattice parameters and crystallite size for the chabazite structure (space group R-3m) were calculated from Rietveld refinement using the program TOPAS (version 5, Bruker AXS, Germany). Crystallite sizes are given as volume-weighted average crystallite size calculated, noted as Lvol-FWHM in TOPAS, from the peaks full width at half maximum (FWHM). Instrument zero shift has been refined for a standard sample and kept constant (at value: 0.00025) for all subsequent refinements, while sample displacement was refined in each fit to account for small sample height differences for different loadings.

Atomic absorption spectroscopy (AAS). The elemental composition of the samples was determined by atomic absorption spectroscopy in a Unicam M Series Flame-AAS equipped with an FS 95 autosampler and a GF 95 graphite furnace.

Helium ion microscopy (HIM). HIM images were obtained using 30 keV He ions with 1.0 pA beam current at normal incidence. Secondary electrons were detected using an Everhart–Thornley detector. For HIM imaging, a very thin layer of carbon (<1 nm) was coated using a carbon sputter deposition system due to the samples being completely insulating. The instrument resolution was 0.35 nm.

Thermogravimetric analysis (TGA). A Netzsch STA 449C Jupiter system was used to conduct TGA and differential scanning calorimetric (DSC) analysis. A typical measurement involved 35 mg of fresh material. The material was heated to 1000°C with a ramping rate of 5°C/min under the flow of 50 ml/min synthetic air and 15 ml/min N_2.

Solid-state NMR measurements. ^{27}Al MAS NMR spectra were collected on a Varian 500 MHz spectrometer using a 4 mm HX probe. Experiments were conducted using a 0.6 µs pulse width, which corresponds to a 9° (π/20) tip angle. Pulse delays of 1 s were applied to fully relax the spins. 5000 scans at a spinning rate of 16 kHz were collected and analysed using MestreNova software. The peaks were referenced externally to a 1.0M $Al(NO_3)_3$ solution set to 0 ppm. To fully hydrate all Al, the samples were stored in a desiccator with saturated $Ca(NO_3)_2$ solution for a minimum of 48 h. Deconvolution of the

spectra was done using a consistent set of Gaussian lineshapes, while allowing the chemical shift (within measure), peak width and peak height to adjust to obtain the least number of squares. An example of a typical deconvoluted spectrum is shown in the Supporting Information (Figure S5).

Gas adsorption (CO_2 and N_2) measurements. Low-temperature nitrogen physisorption measurements were performed on Micromeritics ASAP 2020 to determine the pore volume. The NL-DFT method for N_2 on oxide surfaces without any smoothing was applied to assess the micropore volume. Single point adsorption close to p/p_0 0.99 was applied to determine the total pore volume.

The room temperature (25 °C) CO_2 and N_2 adsorption isotherms of all the SSZ-13 samples were measured using a Micromeritics HPVA100 static volumetric analyser at the setting temperature of 25°C. Prior to the gas adsorption experiment, the chabazite samples were activated at 200°C for a period of 12 h under vacuum and then slowly cooled down to 25°C and the temperature was controlled with a water bath. For low-pressure sorption experiments (up to 1 bar), 100 mbar of the gas was introduced into the sample chamber containing dehydrated SSZ-13 sample every 15 min. After the desorption experiment, the material was degassed for 60 min before using it for the next set of experiments with the second gas (N_2). Only low-pressure experiments were conducted because saturation was already reached at 1 bar.

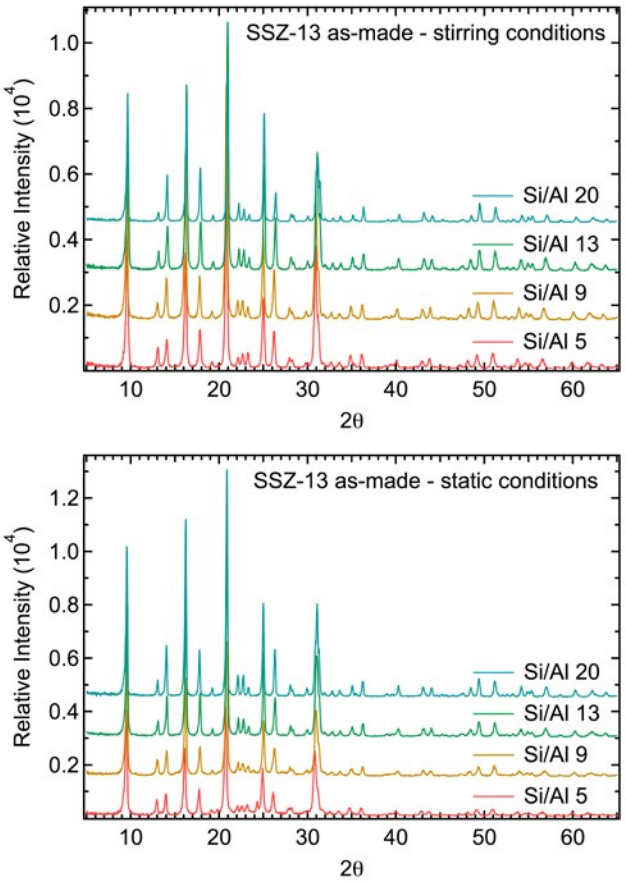

Figure 1. Powder XRD diffractogram of SSZ-13 synthesized under static and stirring conditions. Notice that fully crystalline material is observed and no amorphous background is detected. Colour coding is explained in the legend.

Results & Discussion

Characterization of chabazite SSZ-13

We synthesized the SSZ-13 chabazite zeolite with Si/Al ratios of 5, ~9, ~13, and ~20 as determined by atomic absorption spectroscopy (AAS) using both stirring and static synthesis methods (Table 1). The Si/Al ratio for materials synthesized in static and stirring conditions are in agreement of one another, allowing a direct comparison of the samples.

The materials were characterized in their as-made form by PXRD, as shown in Figure 1. The patterns of calcined materials can be found in the Supporting Information (ESI, Figure S1).

The purity of the synthesized material is clearly visible and all reflections are associated with known references in the literature.[40] No amorphous background is detected, indicating full crystallinity of the material. Removal of the template leads to changes in the intensity of the prominent reflections at 2θ = 9.6°, 16.3°, and 21°. These changes are due to different electron densities in the as-made and calcined material; they are the direct result of removed organic residue affecting the diffraction intensity of the incoming X-rays.[41]

Table 1. Physicochemical properties of the calcined SSZ-13 materials.

Sample	Si/Al[1]	Na/Al[1]	SDA/Al[2]	Unit cell volume[3] [Å^3]	Crystallite size[3] [µm]	Mean particle size[4] [µm]
Si/Al 5 stirring	5.0	0.5	0.3	2409	0.07	0.3
Si/Al 9 stirring	8.9	0.3	0.6	2386	0.06	0.25
Si/Al 13 stirring	13.0	0.3	0.9	2370	0.11	0.5
Si/Al 20 stirring	20.4	0.5	1.4	2355	0.26	2.0
Si/Al 5 static	5.0	0.5	0.3	2412	0.04	8
Si/Al 9 static	8.4	0.5	0.5	2377	0.06	15.5
Si/Al 13 static	12.3	0.3	0.8	2368	0.11	8
Si/Al 20 static	21.9	0.4	1.6	2362	0.34	17

[1]Chemical composition determined by atomic absorption spectroscopy (AAS). Accuracy ± 5wt%. [2]Estimated amounts of template determined by mass loss measured with TGA at temperatures above 200°C. [3]Unit cell volume and crystallite size determined with Rietveld refinement. [4]Mean particle size determined by analysis of 100 particles in helium ion micrographs.

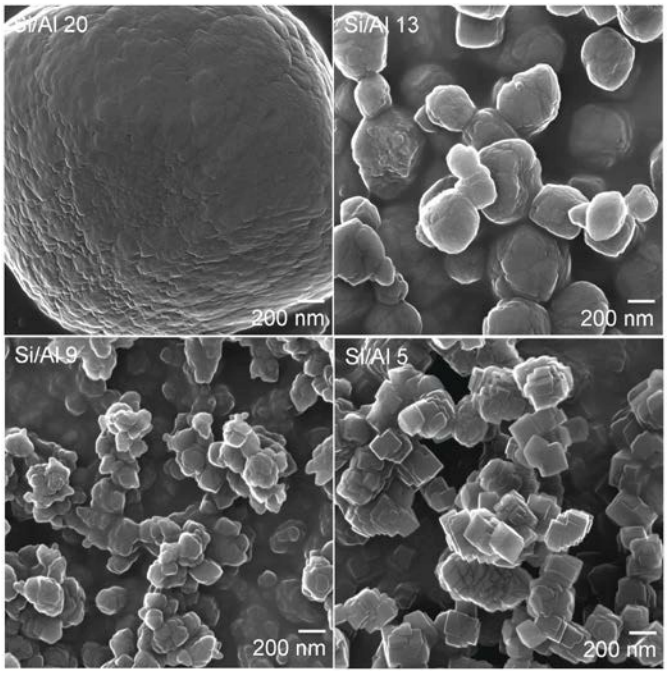

Figure 2. HIM images of SSZ-13 synthesized under stirring conditions with different Al content. High-Si content leads to increased particle size as well as fewer terraces in the morphology of the particles. The large particles are also well separated compared to the remaining samples, which present some degree of intergrowth and agglomeration. The magnifications are listed in the images.

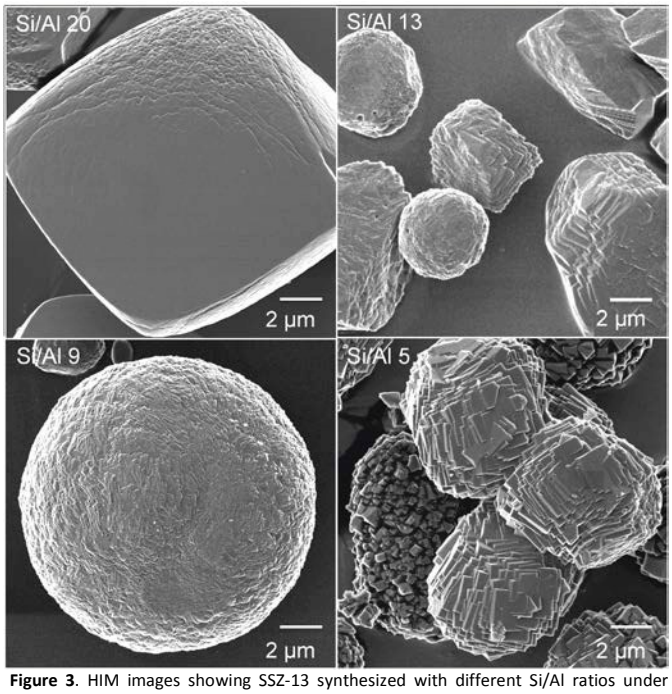

Figure 3. HIM images showing SSZ-13 synthesized with different Si/Al ratios under static conditions. Particles are significantly larger (8-17 µm) than those synthesized under stirring conditions. A larger degree of aluminium incorporation leads to imperfections in the crystal structure shown by the formation of terraces as opposed to smooth surfaces in high-Si samples. Magnifications are reported in the images.

Additionally, decomposition of the template results in small changes (~0.2°) in the 2θ angles to higher values. The 2θ angles are inversely related to the d-spacing between the planes, indicating a smaller unit cell due to the relaxation of the framework. This observation was confirmed by Rietveld refinement, the unit cell volume of calcined materials being shown in Table 1. The expanded unit cell volume of the as-made material is shown in the Supporting Information (ESI, Table S1). Additionally, Rietveld refinement also shows increasing crystallite sizes with increasing Si/Al ratio. The details of Rietveld refinements (Rp, wRp, R_Bragg, GOF) and graphical plots of refined patterns for all the samples are given (ESI, Table S2, Figure S10-S13). The crystallite size is determined by assessing the peak widths and indeed an improved resolution of the doublet at 2θ = 31°, indicating narrower peak width,[41] can be observed for higher silica content materials. Furthermore, increasing unit cell volumes are also observed for increasing amounts of aluminium content. This expansion of the unit cell is due to the longer Al-O bond compared to the Si-O bond.[42] These observations—silica-rich zeolites present narrower peaks and smaller unit cells—can be made for material obtained under both static and stirring conditions.

The difference in particle size was further illustrated when probing the morphology using HIM, as shown in Figures 2 and 3 (ESI, Figure S2). A particle size distribution obtained by measuring the diameter of particles visible in helium ion micrographs and is shown in the Supporting Information (ESI, Figure S3). The largest particles, in agreement with the trend for crystallite size observed from XRD results, are obtained for silica-rich Si/Al 20 with a diameter of 17 µm for SSZ-13 synthesized under static conditions. Besides the obvious changes in particle size, varying the Si/Al ratio also leads to a change in morphology. Zeolite crystal growth mechanisms are complex and several growth types have been proposed.[43, 44] Classically, zeolites grow by layer-by-layer adsorption of growth units, which then migrate to their optimum position such as kink sites. Once a layer is completed, surface nucleation leads to the formation of a new kink site and the crystal growth can continue.[43, 45] The presence of aluminium affects this surface nucleation process. In these synthesized materials, shown in Figures 2 and 3, a high degree of aluminium concentration leads to the formation of terraces with sharp edges as well as a reduction in particle size and crystal domain size. Furthermore, a significant reduction in particle size and a high degree of agglomeration in aluminium-rich samples was observed in SSZ-13 samples synthesized under stirring conditions (Figure 2). Agitation during hydrothermal treatment is known to affect the shape and particle size of zeolite material.[38, 46, 47] It can increase the number of viable nuclei present during the induction period, which is the time required for the localized system to produce crystalline, XRD-detectable material.[47] Agitation can also influence the type of zeolite framework to be formed.[48]

Viable nuclei are a result of germ nuclei, aluminosilicate precursors that continuously aggregate and depolymerize, reaching a critical size in the supersaturated solution.[49] Addition of more structural building units to the viable nuclei will then be energetically favoured and crystal growth occurs, ending the induction period. A larger number of viable nuclei

implies that fewer nutrients are available for crystal growth, resulting in an overall smaller particle size.[49] Under static conditions, supersaturation is not obtained homogeneously for the whole gel, as is the case for stirring conditions. Instead only localized supersaturation is reached and the overall number of viable nuclei is significantly less. However, they have more nutrients available yielding an overall larger particle size. It should be noted, that the material synthesized with a Si/Al 13 ratio under static conditions (Figure 3) is quite heterogeneous. High-silica content material appears to have a cubic shape, whereas low-silica SSZ-13 exhibits more spherical shapes. Si/Al 13 presents a combination of both large irregular cuboid shapes spanning several micrometers and smaller spheroidal particles.

It should be pointed out that there is an apparent discrepancy between the crystallite size determined by Rietveld refinement of X-ray diffractograms and the particle size determined from helium ion microscopy. The crystallite size determined from XRD peaks provides the size of the coherently scattering domains[50], while a single grain observed by microscopy may contain multiple domains that rarely show coherence with each other. The trends for both methods, however, are the same in respect to increasing amounts of aluminium incorporated. Yet there is no clear trend for the crystallite size when comparing different synthesis methods for the same Si/Al ratio. Microscopy reveals vastly different particle sizes; the crystallite size differs only marginally. We attribute this to the limitations of the X-ray diffraction method. X-rays cannot accurately assess the size of polycrystalline aggregates, consisting of several different domains.[50] The static synthesis method, results in much larger particles due to the processes, concerning supersaturation, described above. In addition, the marginal changes to the peak width due to increased crystal size in the micron scale, result in an upper limit for the application of the Rietveld refinement.[50]

The thermal stability of the synthesized SSZ-13 samples was investigated using TGA and DSC analysis. The calorimetric peaks reflect the endo- and exothermic changes occurring in the samples during heating depending on their position and orientation. The decomposition of the organic template can be observed in all samples; it occurred between 400°C and 550 °C and was depicted with large exothermic peaks, as shown in Figure 4. The decomposition temperature of the organic molecule does not change; however, the peak shift of the maxima reflects different degrees of heat flow. If the peak maximum occurs at a low temperature, the template is removed more readily. This is also evident when looking at the onset of mass loss, which correlates with the DSC peak maxima. In the SSZ-13 sample synthesized under static conditions, significant particle size differences affect the temperature at which the template is removed. Larger homogeneous particles such as Si/Al 20 and Si/Al 9 only start decomposing the majority of the template at temperatures above 500°C, whereas the heterogeneous particles of Si/Al 13 and smaller particle sizes of Si/Al 5 have peak maxima up to 100°C lower. In contrast, the stirring materials do not show such dramatic differences in decomposition temperatures, and this is mainly attributed to the improved homogeneity of sample morphology and overall smaller particle size differences.

Nonetheless, the particle size has an effect on template removal and is evident when comparing static and smaller stirring materials. The significant influence of particle size can be explained by looking at the diffusion pathways and morphologies in specific samples. Despite all samples containing similar amounts of template, accessibility, defined by the tortuosity factor[51], and hence facilitation of removal, varies. The diffusion pathway for the exothermic heat flux in large particles is longer, which shifts the maximum to higher temperatures. Additionally, agglomeration in material synthesized under stirring conditions results in mesoporosity, which further contributes to the diffusion pathway. Thus, the agglomerated stirring materials with Si/Al 9 and 13, as seen in Figure 2, have peak maxima at slightly higher temperatures than the well-separated particles with Si/Al 20. Interestingly, the Al-rich sample with Si/Al 5 also readily experiences template decomposition, independent of the synthesis method chosen during synthesis.

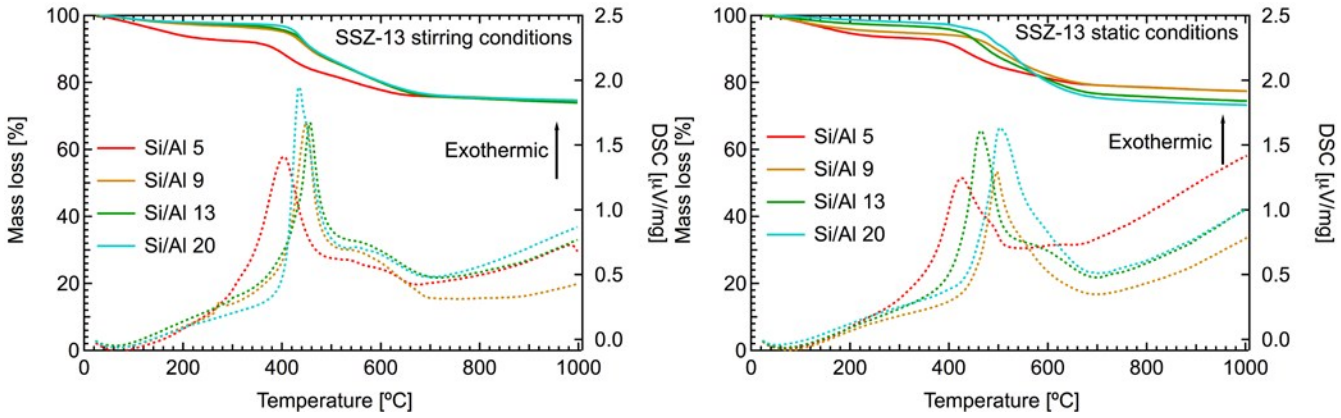

Figure 4. Mass balance and heat flux curves for as-made material synthesized under stirring and static conditions. In both cases, high Al SSZ-13 (Si/Al 5) has the earliest onset of mass loss. The calorimetric curves were not calibrated, thus only the peak location and a general conclusion regarding exothermicity or endothermicity can be drawn. Colour coding is explained in the legend.

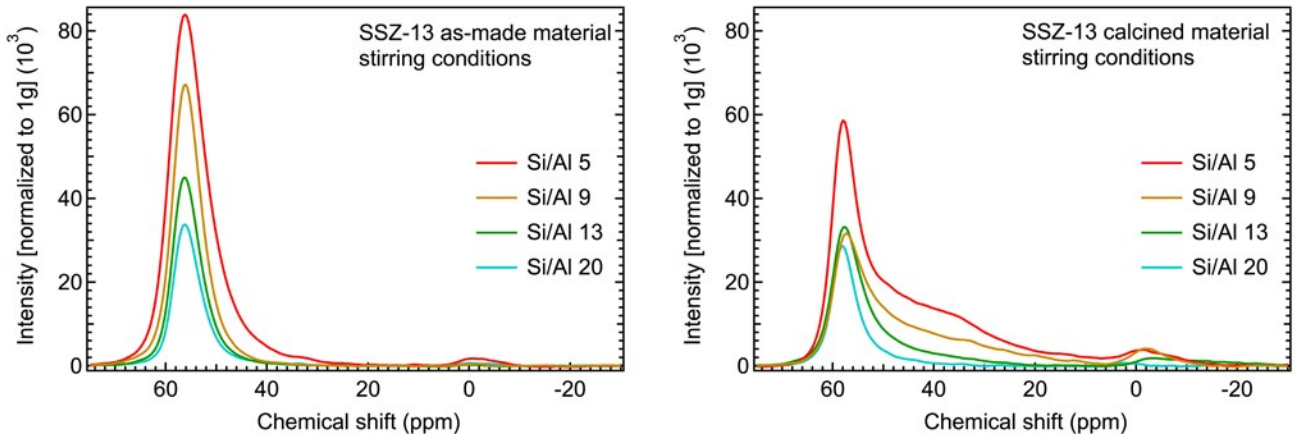

Figure 5. ^{27}Al MAS NMR spectra of as-made and calcined materials synthesized under stirring conditions. The spectra are normalized to 1 g and the differences in intensities reflect varying Al contents (see Table 1). Calcination leads to formation of partially framework-bonded pentahedral Al (40 - 50 ppm) and a higher degree of octahedral Al (0 ppm). Low Si/Al ratios behave more poorly than high Si/Al ratios. Colour coding is reported in the legend

We attribute this to the specific morphology of high-aluminium SSZ-13, which is defined by a large number of terraces and edges. It seems that the diffusion pathway through these terrace structures is shorter than for the corresponding agglomerated and larger, high-silica SSZ-13 samples. It should be noted that all samples, especially hydrophilic Al-rich materials, tend to lose additional mass at even lower temperatures due to adsorbed water. The amount of template incorporated in the as-made material ranges from 16-24 wt% which is given as a ratio between the structure directing agent and Al (SDA/Al) in Table 1. It ranges from 0.3 to 1.6. This was determined by assessing the mass loss at temperatures above 200°C to eliminate the contribution of adsorbed water. Al-rich samples lie at the lower end, only 0.3 molecules of $TMAde^+$ per Al being found in the sample. High Si/Al ratios result in a significantly higher SDA/Al ratio of up to 1.6. This is contributed to the presence of occluded neutral species required for the formation of the CHA structure. The Na content, in the form of Na/Al, is found to be around 0.5 for all samples, despite the Si/Al ratio. The remaining Al atoms are therefore charge balanced by $TMAde^+$ cations.

Another method of characterization was ^{27}Al MAS NMR; the results are presented in Figure 5, both for as-made and calcined forms obtained under stirring conditions. The spectra for static material can be found in the supporting information (ESI, Figure S4). The quantitative spectra are normalized to 1 g with the changes in intensity nicely reflecting varying Si/Al ratios. There is significant line broadening for Al-rich samples, reflecting the higher degree of disorder in agreement with and already adressed by XRD, HIM, and TGA characterization results. Simple line fitting using gaussian line shapes allowed us to make assessments on the contribution of different Al coordination sites. An example of a typically deconvoluted spectrum is shown in the Supporting Information (ESI, Figure S5) and the resulting Al distribution is shown in Figure 6. Due to the quadrupolar nature of aluminium some can be broadened beyond detection.[52, 53] Higher field strenghts can

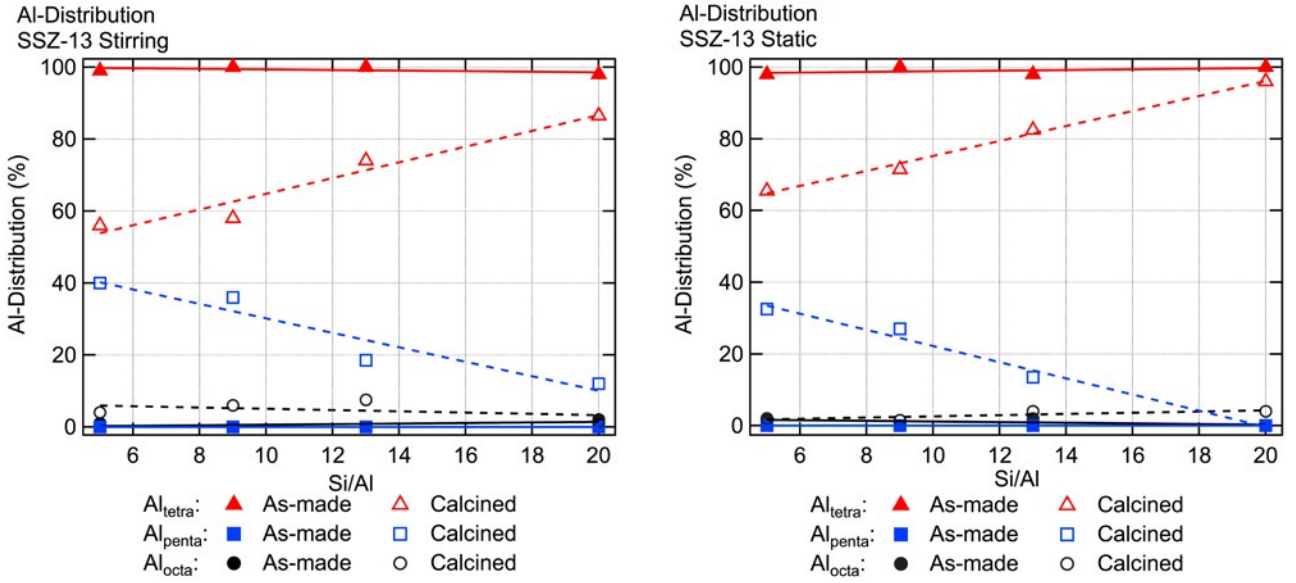

Figure 6. Distribution of varying Al coordination sites in the prepared samples. The individual contribution was determined by deconvoluting the ^{27}Al MAS NMR spectra.

minimize these quadrupolar interactions.[53, 54] The field strength used in our experiments required interpretation of the data under the assumption that all aluminium is fully hydrated and equally visible. Essentially, all aluminium is in tetrahedral framework position for the as-made materials; the signal appears at 57-58 ppm. There are only traces of octahedral extra-framework aluminium (0 ppm). Removal of the template requires high temperatures, seen in the TGA/DSC results, which leads to distortion and partial breaking of the Al-O- bonds of tetrahedral aluminium. As a result, it is now only partially bonded to the framework with one or more hydroxyls or water molecules balancing its positive charge. It is penta-coordinated giving rise to a broad signal between 30-50 ppm. The high silica SSZ-13 samples are less prone to this partial dealumination process, illustrated by the clear trend in Figure 6. Calcination also leads to a change in the chemical shift of the tetrahedral position by several parts per million (~2 ppm). Chemical shielding is affected by the removal of organic residue. A downfield shift indicates less shielding as a result of the environment surrounding the investigated aluminium becoming electron-poor due to the removal of the template.

Gas adsorption studies

The nitrogen adsorption measurements of the chabazite materials at -196 °C provide insight into the overall pore volume of SSZ-13 zeolites for all Si/Al ratios and synthesis method (Table 2, ESI, Figure S6). Additionally, a pore size distribution (PSD) for the microporous regime (< 2 nm) can be found in the Supporting Information (ESI, Figure S7). The PSD clearly reflects the internal dimensions of the CHA framework, with only pore sizes between 0.6 and 1.0 nm being filled. It is in agreement with the dimensions of the ellipsoidal CHA cage.[34] There is also a clear trend visible when assessing the micropore volume. In both static and stirring materials the micropore volume increases with increasing Si/Al ratio (Table 2). We attribute this to the decreased unit cell volume and increasing crystallite size determined from Rietveld refined XRD data. This allows for a higher packing density and subsequent pore volume. The mesoporous contribution to the majority of samples is only marginal.

Table 2. Pore sizes, and CO_2 uptake for calcined SSZ-13 synthesized under static and stirring conditions. Overall, the pore volumes in both the static and stirring material reflect the particle size and morphology.

Sample	Micropore volume [cm^3/g]	Total pore volume * [cm^3/g]	CO_2 uptake [mmol/g]
Si/Al 5 stirring	0.27	0.31	4.8
Si/Al 9 stirring	0.27	0.48	3.7
Si/Al 13 stirring	0.29	0.36	3.7
Si/Al 20 stirring	0.32	0.33	3.5
Si/Al 5 static	0.21	0.22	4.3
Si/Al 9 static	0.21	0.21	3.0
Si/Al 13 static	0.26	0.28	3.0
Si/Al 20 static	0.26	0.29	3.1

*determined with single point adsorption close to p/p_0 0.99.

The exceptions are SSZ-13 synthesized in stirring conditions with a Si/Al ratio of 9 and 13. The N_2 isotherm is defined by a significant hysteresis loop at high partial pressures, an indication for intercrystalline mesopores. A result of the high degree of agglomeration observed with HIM. In addition, the overall smaller particle sizes resulting from synthesis in stirring conditions leads to a larger overall pore volume.

Based on the size and geometry of guest molecules and host zeolite, CO_2 (kinetic diameter: 3.33 Å) and N_2 (kinetic diameter: 3.64 Å)[55] can readily diffuse into the SSZ-13 pore structure with a pore aperture of 3.8 Å.[37] Besides the size, CO_2 molecules also possess a higher polarizability (26.5 X 10^{-25} cm^3) and electric quadrupole moment (4.3 X 10^{-26} $esu.cm^2$), which result in stronger interaction with the host framework.[56] Grand-Canonical Monte Carlo simulation studies by Bell et al. revealed dispersive interactions to be the primary contribution to CO_2 adsorption in CHA.[57, 58] These interactions are determined by the distance between C_{CO2}, O_{CO2}, and the oxygen atoms of the framework (O_{CHA}). The strongest dispersive interactions were calculated for 3.44 Å ($O_{CO2} - O_{CHA}$) and 3.30 Å ($C_{CO2} - O_{CHA}$), and contact distances below 4 Å had attractive van der Waals interactions.[57, 58] This helped Bell et al. determine the location of two adsorption sites for CO_2, one in the 8MR window and the other one located in ellipsoidal cage of the SSZ-13 framework.

Additionally, cations, charge balancing the negative framework charge, are also found to contribute to the CO_2 adsorption properties of the zeolite.

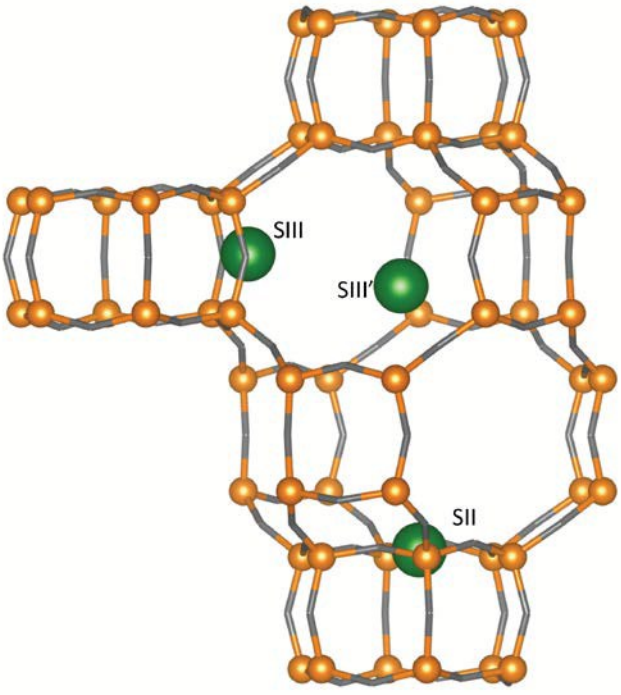

Figure 7. Illustration of a partial CHA framework structure consisting of three DR6 units and the resulting CHA cage. Possible sites for cations are marked as SII, SIII, and SIII'. Adapted with permission from Pham, T. D.; Liu, Q.; Lobo, R. F. *Langmuir* **2013**, *29*, 832-839. Copyright 2016 American Chemical Society.

Lobo et al. performed a detailed investigation of CO_2 adsorption in chabazite zeolites using in-situ neutron and XRD methods and revealed molecular insights and the preferred location of adsorption sites in alkali-exchanged chabazites and varied aluminium content.[35] Cations act as hard Lewis acids for the Lewis basic oxygen in CO_2. Therefore, it is important to define possible sites for cation occupancy, illustrated in Figure 7. Depending on the size of the cation, as well as the concentration of cations in the unit cell, several sites can be identified.[33, 59, 60] One site is located in the window of the DR6 (SII), and two sites are in the 8MR windows, one close to the connecting four-membered ring (SIII) and the other in the centre of the 8MR (SIII'). In this study, both particle size and specific morphology influenced by Si/Al ratio affect the porous properties of the SSZ-13 materials and can be clearly seen from the room temperature CO_2 and N_2 sorption studies. The CO_2 and N_2 uptake measurements at 25°C were performed on all the SSZ-13 samples (Si/Al 5, 9, 13 and 20) synthesized using both stirring and static methods.

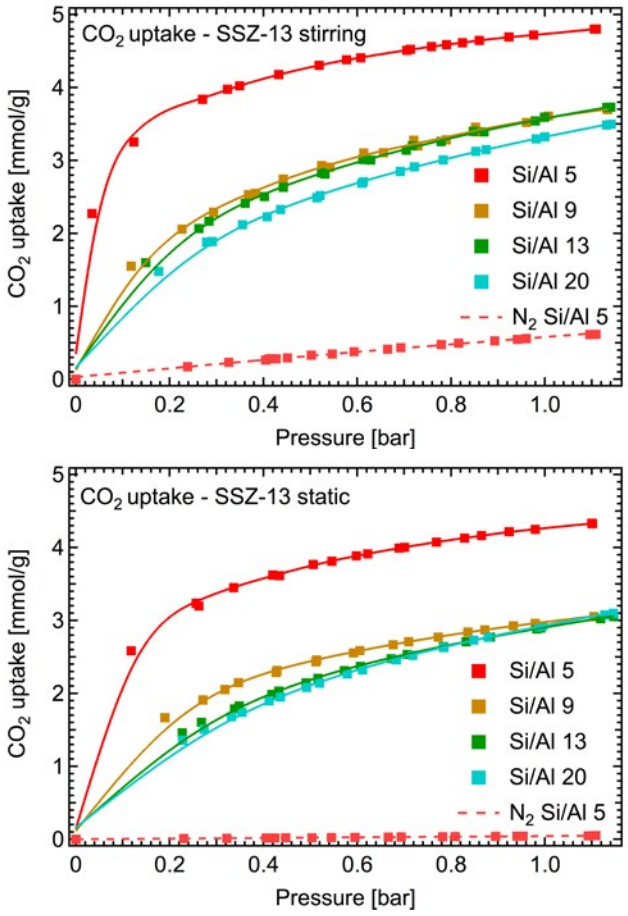

Figure 8. CO_2 and N_2 gas sorption studies of SSZ-13 chabazite materials with various Si/Al ratios synthesized under stirring conditions (top) and static (bottom) conditions.

The adsorbed amount of CO_2 per gram of material was plotted against the pressure (Figure 8). In line with the increasing aluminium content in the SSZ-13 framework, the CO_2 adsorption capacities also increased. At 1 bar, the CO_2 uptake in Al-rich SSZ-13 (Si/Al 5) showed a maximum, while the lowest CO_2 sorption capacities were found for the samples with low aluminium content (Si/Al 20). As expected, a similar trend was observed in materials synthesized under both stirring and static conditions. In both cases, the Al-rich SSZ-13 showed the highest uptake of CO_2. It is a well-known phenomenon that the adsorption capacity and selectivity of zeolites for the polar molecules increases when the Si/Al ratio decreases.[61] This is mainly due to the increased number of charged sites and surface basicity caused by the respective substitution of Si^{4+} ions by Al^{3+} ions. Plotting the adsorption capacity against the Si/Al ratio further highlights the significant correlation between uptake capacity and charge density, as seen in Figure 9.

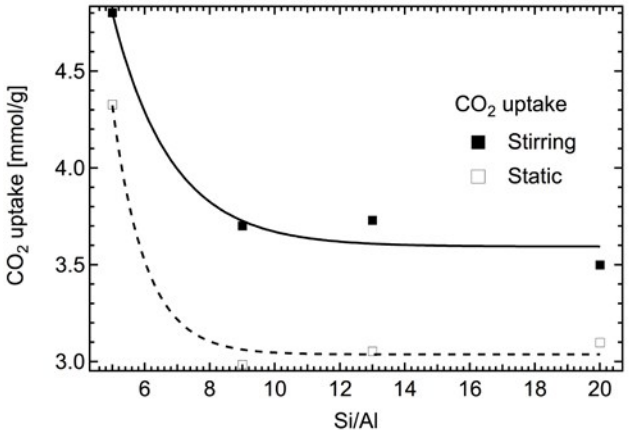

Figure 9. Illustration of the CO_2 uptake dependence on the Al content. High Al densities (2.4 atoms per unit cell) increase the CO_2 uptake drastically.

Nitrogen adsorption is dependent upon the strength of the electric field in the zeolite framework and is observed to be very low, similar to that of other zeolites reported in the literature (ESI, Figure S8).[33] However, the adsorption trends for CO_2 in a zeolite framework are more intricate due to carbon in CO_2 being a Lewis acid, while bridging oxygen atoms interacting with alkali cations act as Lewis bases. Additionally, as was already mentioned, the cations act as Lewis acids for the Lewis basic oxygen in CO_2. Therefore, the adsorption is dependent on dispersive physical interactions and stronger chemical interactions. They are mainly governed by the Si/Al ratio, as well as type of alkali cation and its location inside the framework.[62] By increasing the Si/Al ratio in the material, the number of aluminium atoms decreases from approximately 2.4 atoms per unit cell in the case of Si/Al 5 sample to c.a. 1.3 (Si/Al 9), 0.9 (Si/Al 13), and further 0.6 (Si/Al 20), respectively. Each aluminium atom needs to be charge balanced by a cation. In the investigated materials only sodium ions and protons are present, the latter due to decomposition of the organic template. Protons are very weak Lewis acids, thus mostly sodium ions play a role in CO_2 adsorption. Therefore, the framework oxygen in Al-rich SSZ-13 samples, bonded to these sodium cations has a more basic character that results in a strong adsorbate (zeolite)—adsorbent (CO_2) interaction via dipole-induced-dipole interactions leading to chemisorption.[33] This can be seen in the case of Si/Al 5 where high CO_2 loading

is reached at very low pressures. As the number of cations per unit cell decreases at increasing Si/Al ratios (e.g., Si/Al 9), the adsorbate-adsorbent interaction only dominates in very low-pressure regions, as can be seen by a higher CO_2 uptake initially. At pressures reaching 1 bar, adsorbate-adsorbate interactions become more important. Further reduction of the Al content (Si/Al 13 and 20) and consequently cation content leads to the overall basic character of the framework becoming negligible. Smaller dispersion interaction energies between adsorbate and adsorbent results in lower CO_2 adsorption capacities observed for Si/Al 13 and 20. It is interesting to note that the Si/Al 9, Si/Al 13, and Si/Al 20 samples have similar adsorption profiles. This can be attributed to a combination of weak chemisorption due to the scarcity of Na^+ ions in the lattice and the resulting increase in available pore volume. An increased pore volume enables more CO_2 to be adsorbed with the effect being cancelled out by a weaker chemisorption. This yields similar adsorption profiles for Si/Al 9, Si/Al 13, and Si/Al 20 in both stirring and static cases.

Extensive reports are available in the literature on the effect of pore size; however, the effect of particle size on gas adsorption properties has rarely been investigated. In this study, apart from the Si/Al ratio, the effect of agitation made a significant change in the textural properties of SSZ-13 samples, as discussed above. Specifically, when hydrothermal synthesis was performed with stirring an overall smaller particle size of ~250 nm was obtained. The particles with smaller size will have a large density of surface sites and improved gas diffusivity.[63, 64] For reference, at 1 bar pressure, the stirred sample (Si/Al 5) shows a higher CO_2 uptake of 4.8 mmol/g than the same composition obtained under static conditions at ~4.32 mmol/g at 1 bar (Figure 10). As a note in passing, Lobo et al. report a CO_2 uptake value of 5 mmol/g for a fully exchanged Na-SSZ-13 of similar chemical composition to our material.[33] The discrepancy can be explained by the presence of weak Lewis acidic protons in our material.

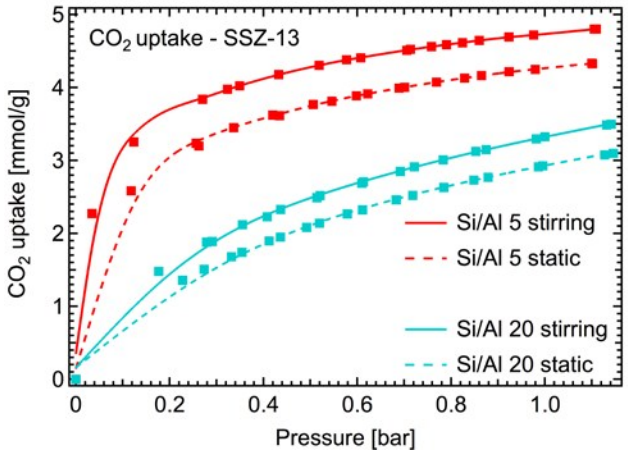

Figure 10. Comparison of CO_2 sorption studies in SSZ-13 (Si/Al = 5 and 20) synthesized under stirring and static conditions. The increased sorption trend was observed in all of the stirred samples when compared to the Si/Al ratios of the static samples.

All samples synthesized under stirring conditions show superior CO_2 adsorption when compared to larger particles of the same chemical composition obtained in static conditions. This is mainly due to the increased amount of micropore volume, resulting in more active sites crucial for CO_2 adsorption. For reference, the differences in the increased CO_2 sorption capacities in SSZ-13 samples of various Si/Al ratios (5 and 20) under stirring and static conditions were shown in Figure 10 (ESI, Figure S9). It should also be noted that all samples showed very little (if any) uptake of N_2 in either the stirred or static samples (ESI, Figure S8).

Conclusions

The thermally stable SSZ-13 zeolite showed superior CO_2 sorption characteristics. The CO_2 adsorption isotherms clearly showed the role of aluminium content in the chabazite framework. This can affect the generated Lewis basicity of the framework oxygen as well as cation concentration, both important factors in the interaction of CO_2 and the adsorbent. Accordingly, the Al-rich SSZ-13 (Si/Al 5) showed the highest CO_2 sorption capacities, while Si-rich SSZ-13 (Si/Al 20) showed the lowest. In addition, particle size played a role in CO_2 sorption capacities; the smaller ~250 nm sized particles showed the highest sorption capacity compared to larger 17 µm sized particles with the same Si/Al composition. This is mainly due smaller particles having a larger density of surface sites, due to increased microporous contribution, available for CO_2 adsorption.

Acknowledgements

S.P and M.D. thank the Pacific Northwest National Laboratory's (PNNL's) Laboratory Directed Research and Development program for the support of this study. We thank V. Shutthanandan for HIM characterization, which was performed at the Environmental Molecular Sciences Laboratory, a national scientific user facility sponsored by the U.S. Department of Energy's Office of Biological and Environmental Research, located at PNNL. PNNL is operated by Battelle for the U.S. Department of Energy under Contract DE-AC05-76RL01830. Further, we would like to acknowledge M. Neukamm from the Technical University of Munich, who performed the atomic absorption spectroscopy.

Abbreviations

XRD, X-ray diffraction; MAS, magic angle spinning; NMR, nuclear magnetic resonance.

Notes and references

† Electronic Supplementary Information (ESI) available: PXRD patterns, HIM images, particle size distribution, ^{27}Al MAS NMR spectra, N_2 physisorption isotherms and pore size distributions, as

well as CO_2 and N_2 adsorption measurements. See DOI: 10.1039/c000000x/

1. S. F. Pan, H. Q. Tian, S. R. S. Dangal, Q. C. Yang, J. Yang, C. Q. Lu, B. Tao, W. Ren and Z. Y. Ouyang, *Earth's Future*, 2015, **3**, 15-35.
2. D. M. D'Alessandro, B. Smit and J. R. Long, *Angew. Chem. Int. Ed.*, 2010, **49**, 6058-6082.
3. R. G. Watts, *Abstr Pap Am Chem S*, 1981, **182**, 26-Petr.
4. Y. S. Bae and R. Q. Snurr, *Angew. Chem. Int. Ed. Engl.*, 2011, **50**, 11586-11596.
5. B. J. P. Buhre, L. K. Elliott, C. D. Sheng, R. P. Gupta and T. F. Wall, *Prog. Energy Combust. Sci.*, 2005, **31**, 283-307.
6. G. T. Rochelle, *Science*, 2009, **325**, 1652-1654.
7. D. J. Heldebrant, C. R. Yonker, P. G. Jessop and L. Phan, *Energy Environ. Sci.*, 2008, **1**, 487-493.
8. R. K. Motkuri, P. K. Thallapally, B. P. McGrail and S. B. Ghorishi, *CrystEngComm*, 2010, **12**, 4003-4006.
9. P. Ramakrishnan and S. Shanmugam, *RSC Adv.*, 2014, **4**, 59633-59636.
10. M. T. Conato, M. D. Oleksiak, B. P. McGrail, R. K. Motkuri and J. D. Rimer, *Chem. Commun.*, 2015, **51**, 269-272.
11. P. K. Thallapally, J. Tian, R. K. Motkuri, C. A. Fernandez, S. J. Dalgarno, P. B. McGrail, J. E. Warren and J. L. Atwood, *J. Am. Chem. Soc.*, 2008, **130**, 16842-16843.
12. S. Saha, S. Chandra, B. Garai and R. Banerjee, *Indian J. Chem., Sect A*, 2012, **51**, 1223-1230.
13. P. Nugent, Y. Belmabkhout, S. D. Burd, A. J. Cairns, R. Luebke, K. Forrest, T. Pham, S. Q. Ma, B. Space, L. Wojtas, M. Eddaoudi and M. J. Zaworotko, *Nature*, 2013, **495**, 80-84.
14. Z. J. Zhang, Z. Z. Yao, S. C. Xiang and B. L. Chen, *Energy Environ. Sci.*, 2014, **7**, 2868-2899.
15. C. S. Cundy and P. A. Cox, *Chem Rev*, 2003, **103**, 663-702.
16. R. M. Barrer, *Zeolite and Clay Minerals*, Academic Press, New York, 1978.
17. S. Kesraoui-Ouki, C. R. Cheeseman and R. Perry, *J. Chem. Technol. Biotechnol.*, 1994, **59**, 121-126.
18. A. Corma, *Chem Rev*, 1997, **97**, 2373-2420.
19. J. Sublet, M. Pera-Titus, N. Guilhaume, D. Farrusseng, L. Schrive, P. Chanaud, B. Siret and S. Durecu, *Aiche J*, 2012, **58**, 3183-3194.
20. S. T. Yang, J. Kim and W. S. Ahn, *Microporous Mesoporous Mater.*, 2010, **135**, 90-94.
21. S. Smeets, D. Xie, L. B. McCusker, C. Baerlocher, S. I. Zones, J. A. Thompson, H. S. Lacheen and H. M. Huang, *Chem. Mater.*, 2014, **26**, 3909-3913.
22. R. K. Motkuri, H. V. R. Annapureddy, M. Vijaykumar, H. T. Schaef, P. F. Martin, B. P. McGrail, L. X. Dang, R. Krishna and P. K. Thallapally, *Nat Commun*, 2014, **5**, 4368.
23. T. Watanabe and D. S. Sholl, *Langmuir*, 2012, **28**, 14114-14128.
24. R. K. Motkuri, P. K. Thallapally, H. V. Annapureddy, L. X. Dang, R. Krishna, S. K. Nune, C. A. Fernandez, J. Liu and B. P. McGrail, *Chem. Commun.*, 2015, **51**, 8421-8424.
25. Z. J. Zhang, Y. G. Zhao, Q. H. Gong, Z. Li and J. Li, *Chem Commun*, 2013, **49**, 653-661.
26. T. H. Bae, M. R. Hudson, J. A. Mason, W. L. Queen, J. J. Dutton, K. Sumida, K. J. Micklash, S. S. Kaye, C. M. Brown and J. R. Long, *Energy Environ. Sci.*, 2013, **6**, 128-138.
27. J. A. Mason, K. Sumida, Z. R. Herm, R. Krishna and J. R. Long, *Energy Environ. Sci.*, 2011, **4**, 3030-3040.
28. K. T. Chue, J. N. Kim, Y. J. Yoo, S. H. Cho and R. T. Yang, *Ind Eng Chem Res*, 1995, **34**, 591-598.
29. J. van den Bergh, M. Mittelmeijer-Hazeleger and F. Kapteijn, *J. Phys. Chem. C*, 2010, **114**, 9379-9389.
30. F. N. Ridha and P. A. Webley, *Sep Purif Technol*, 2009, **67**, 336-343.
31. R. Krishna and J. M. van Baten, *J. Membr. Sci.*, 2010, **360**, 323-333.
32. M. R. Hudson, W. L. Queen, J. A. Mason, D. W. Fickel, R. F. Lobo and C. M. Brown, *J. Am. Chem. Soc.*, 2012, **134**, 1970-1973.
33. T. D. Pham, Q. Liu and R. F. Lobo, *Langmuir*, 2013, **29**, 832-839.
34. T. D. Pham, R. Xiong, S. I. Sandler and R. F. Lobo, *Microporous Mesoporous Mater.*, 2014, **185**, 157-166.
35. T. D. Pham, M. R. Hudson, C. M. Brown and R. F. Lobo, *ChemSusChem*, 2014, **7**, 3031-3038.
36. B. P. C. Hereijgers, F. Bleken, M. H. Nilsen, S. Svelle, K.-P. Lillerud, M. Bjørgen, B. M. Weckhuysen and U. Olsbye, *J Catal*, 2009, **264**, 77-87.
37. D. W. Fickel and R. F. Lobo, *The Journal of Physical Chemistry C*, 2010, **114**, 1633-1640.
38. Z. Bohström, B. Arstad and K. P. Lillerud, *Micropor Mesopor Mat*, 2014, **195**, 294-302.
39. F. Gao, N. M. Washton, Y. Wang, M. Kollár, J. Szanyi and C. H. F. Peden, *J Catal*, 2015, **331**, 25-38.
40. C. Baerlocher and L. B. McCusker, Database of Zeolite Structures, http://www.iza-structure.org/databases/, (accessed October, 2015).
41. L. B. McCusker and C. Baerlocher, in *Stud. Surf. Sci. Catal.*, eds. J. Čejka and H. v. Bekkum, Elsevier, 2005, vol. 157, pp. 41-64.
42. E. A. Eilertsen, B. Arstad, S. Svelle and K. P. Lillerud, *Microporous Mesoporous Mater.*, 2012, **153**, 94-99.
43. C. S. Cundy and P. A. Cox, *Microporous Mesoporous Mater.*, 2005, **82**, 1-78.
44. M. Kumar, H. Luo, Y. Román-Leshkov and J. D. Rimer, *J Am Chem Soc*, 2015, DOI: 10.1021/jacs.5b07477.
45. C. S. Cundy, in *Stud. Surf. Sci. Catal.*, eds. J. Čejka and H. v. Bekkum, Elsevier, 2005, vol. 157, pp. 65-90.
46. K. Kosuge, T. Sato, N. Kikukawa and M. Takemori, *Chem Mater*, 2004, **16**, 899-905.
47. L. Ding, Y. Zheng, Z. Zhang, Z. Ring and J. Chen, *Micropor Mesopor Mat*, 2006, **94**, 1-8.
48. M. Derewinski and M. Machowska, in *Stud. Surf. Sci. Catal.*, eds. E. van Steen, I. M. Claeys and L. H. Callanan, Elsevier, 2004, vol. Volume 154, Part A, pp. 349-354.
49. E. J. P. Feijen, J. A. Martens and P. A. Jacobs, in *Preparation of Solid Catalysts*, Wiley-VCH Verlag GmbH, 2008, DOI: 10.1002/9783527619528.ch3k, pp. 262-284.
50. A. W. Burton, K. Ong, T. Rea and I. Y. Chan, *Microporous Mesoporous Mater.*, 2009, **117**, 75-90.
51. G. Leofanti, M. Padovan, G. Tozzola and B. Venturelli, *Catal Today*, 1998, **41**, 207-219.
52. J. A. van Bokhoven, A. L. Roest, D. C. Koningsberger, J. T. Miller, G. H. Nachtegaal and A. P. M. Kentgens, *J. Phys. Chem. B*, 2000, **104**, 6743-6754.
53. E. Lippmaa, A. Samoson and M. Magi, *J. Am. Chem. Soc.*, 1986, **108**, 1730-1735.

54. C. A. Fyfe, J. L. Bretherton and L. Y. Lam, *J. Am. Chem. Soc.*, 2001, **123**, 5285-5291.
55. G. Aguilar-Armenta, G. Hernandez-Ramirez, E. Flores-Loyola, A. Ugarte-Castaneda, R. Silva-Gonzalez, C. Tabares-Munoz, A. Jimenez-Lopez and E. Rodriguez-Castellon, *J Phys Chem B*, 2001, **105**, 1313-1319.
56. T. C. Golden and S. Sircar, *J. Colloid Interface Sci.*, 1994, **162**, 182-188.
57. M. Fischer and R. G. Bell, *J. Phys. Chem. C*, 2013, **117**, 17099-17110.
58. M. Fischer and R. G. Bell, *J. Phys. Chem. C*, 2012, **116**, 26449-26463.
59. L. J. Smith, H. Eckert and A. K. Cheetham, *J Am Chem Soc*, 2000, **122**, 1700-1708.
60. B. Civalleri, A. M. Ferrari, M. Llunell, R. Orlando, M. Mérawa and P. Ugliengo, *Chem Mater*, 2003, **15**, 3996-4004.
61. G. Calleja, J. Pan and J. A. Calles, *J. Chem. Eng. Data*, 1998, **43**, 994-1003.
62. D. Bonenfant, M. Kharoune, P. Niquette, M. Mimeault and R. Hausler, *Sci Technol Adv Mat*, 2008, **9**.
63. M. E. Davis and R. J. Davis, *Fundamentals of chemical reaction engineering*, Courier Corporation, 2012.
64. M. Auffan, J. Rose, J.-Y. Bottero, G. V. Lowry, J.-P. Jolivet and M. R. Wiesner, *Nat. Nanotechnol.*, 2009, **4**, 634-641.

Table of content graphic and text for

Impact of chabazite SSZ-13 textural properties and chemical composition on CO_2 adsorption applications

Sebastian Prodinger,[a] Rama Sesha Vemuri,[b] Tamas Varga,[c] B. Peter McGrail,[b] Radha Kishan Motkuri,[b,*] and Miroslaw A. Derewinski,[a,*]

[a.] Institute for Integrated Catalysis, Physical Sciences Division, Pacific Northwest National Laboratory (PNNL), Richland, Washington 99352. E-mail: Miroslaw.Derewinski@pnnl.gov

[b.] Hydrocarbon Processing Group, Energy and Environment Directorate, Pacific Northwest National Laboratory (PNNL), Richland, WA 99352, USA. E-mail: Radhakishan.Motkuri@pnnl.gov

[c.] Environmental Molecular Sciences Laboratory, Pacific Northwest National Laboratory (PNNL), Richland, WA 993542, USA.

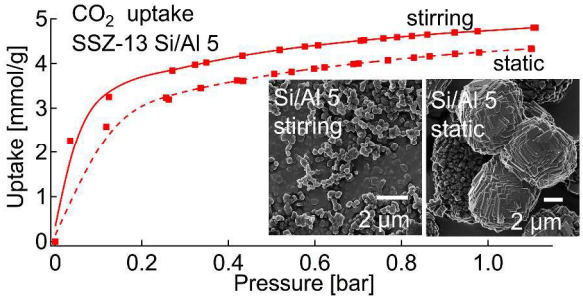

A narrow pore zeolite was synthesized with different Si/Al ratio and micro to nano particle size where both played an important role in CO_2 adsorption.